Energy Reports 8 (2022) 7870–7883

Contents lists available at ScienceDirect

Energy Reports

journal homepage: www.elsevier.com/locate/egyr

Experimental characterization of the temperature gradient inside a membrane distillation module

Marie-Alix Dalle *, Filip Janasz, Stephen Leyer

University of Luxembourg, Faculty of Science, Technology and Medicine, 6, rue Richard Coudenhove-Kalergi 1356, Luxembourg

ARTICLE INFO

Article history:
Received 13 January 2022
Received in revised form 1 June 2022
Accepted 6 June 2022
Available online xxxx

Keywords:
Water desalination
Low-tech
Membrane distillation
Temperature gradient

ABSTRACT

One of the solutions to the current fresh water challenge is desalination using low-grade heat (solar radiation or waste heat), such as Air-gap Membrane Distillation (AGMD). Based on evaporation, induced by a temperature gradient across a hydrophobic membrane, this process has an improved energy efficiency thanks to the inclusion of the air-gap by limiting the heat losses, while hindering the mass transfer at the same time. Understanding of the temperature distribution in the module is crucial for working towards improved efficiency and freshwater output.

This work describes a setup and optical measurement method dedicated to analysis of energy and mass transfer resistances through temperature gradient measurement in the bulk and observation of boundary layer at the membrane. In particular data acquisition, processing and interpretation framework is presented, and compared to existing literature. Initial results indicate that the method is successful, although a number of improvements are proposed to address the identified shortcomings.

1. Introduction

Due to a combination of climate change and population growth, fresh water is becoming a limited resource, even entering the commodity market in 2020 (Chipman, 2020) .

Because 97 percent of the world's water is salty (CNRS, 2013), desalination is an obvious answer to future supply issues. Currently, the most extensively used desalination systems such as Reverse Osmosis (RO), Multiple Effects (ME) or Multiple Flash Stages (MSF) require high pressure or high temperature to operate. These translate to high energy demand and operation costs, unaffordable to some developing countries where water shortages are most severe (Bandelier, 2016).

Membrane Distillation (MD) is a viable alternative using low-grade heat which can be harvested directly from solar radiation of from industrial waste heat. It also works well with recycled water and even highly concentrated brine. Distillation has recently regained interest thanks to hydrophobic porous membranes developed for RO. By allowing to increase the vapor pressure differential these membranes improve MD modules output, making them a more attractive solution. Nevertheless, even with improved output, MD is still not competitive on the market against RO, MSF, and ME.

Various techniques can be set to establish the vapor pressure differential driving the evaporation process (Lawson and Lyold, 1997; Alkhudhiri et al., 2012).

The energy forms used in MD are heat, to sustain evaporation, and mechanical work powering water feed and coolant flows, as well as external condensers in case of VMD or SGMD. However, the amount of heat required for evaporation far outweighs the power required for circulation (Swaminathan et al., 2015). Hence the parameter used to compare the energy efficiency of the different configurations is the dimensionless Gain Output Ratio (GOR), defined as the ratio of the thermal energy required to vaporize the mass of water produced to the thermal energy input actually provided to the system (Saffarini et al., 2012). Inlet hot and cold water flow temperatures, feed flow rate, and air-gap thickness all affect this ratio (Summers et al., 2012; He Li et al., 2014). Higher values indicate a more efficient process. VMD can reach a maximum GOR of 1 (Swaminathan et al., 2015), while SGMD' GOR is limited to 4, and DCMD and AGMD can achieve even slightly higher values, with AGMD having an advantage (Criscuoli, 2016).

The AGMD process was chosen for this study, due to its low energy consumption and high energy efficiency. The downside of this process is that the air-gap hinders mass transfer and hence reduces fresh water output flow. A balance between energy efficiency and output flow production has to be found.

MD's output flow depends on a partial water vapor pressure at the cold side of the membrane and on the energy flux at the hot water membrane interface (Persad, 2014). To improve the output flow, more thermal energy must be provided to the membrane interface. This energy flow, observable as a temperature differential

* Corresponding author.
E-mail addresses: marie-alix.dalle@uni.lu (M.-A. Dalle), Filip.janasz@uni.lu (F. Janasz), Stephen.leyer@uni.lu (S. Leyer).

https://doi.org/10.1016/j.egyr.2022.06.011

between water bulk and membrane interface, must be quantified in order to provide accurate performance prediction (Suleman et al., 2021).

Most research about membrane distillation focus on DCMD (Saffarini et al., 2012). In addition most experiments actually investigating AGMD only monitor inlet and outlet temperatures and feed water and coolant pressures, along with the output flow (Liu et al., 1998; Kurokawa et al., 1990; Banat and Simandl, 1994; Xu et al., 2016a; Alsalhy et al., 2013; Mokhtar et al., 2019).

Several research groups investigated measurements of the temperature distribution inside the module. It has been achieved by interpolating local measurements using thermocouples evenly distributed on the hot and cold channel walls and membrane surface (Janajreh et al., 2017), without measuring the continuous temperature profile across the hot water channel. Alternatively, thermochromic liquids have been used to quantify the temperature distribution at the membrane surface to assess the impact of spacers (Tamburini et al., 2015) .

Kroiß et al. (2014) measured thermal and concentration profiles across the feed flow in RO. Although the authors claimed this approach can be used on MD, it has not yet been tested directly.

No continuous monitoring of fluid thermal and concentration polarization across the hot channel or air-gap has yet been attempted in an AGMD module. However, this data is crucial to correctly model the evaporation process, and energy transport. It would be also essential for validation of numerical methods that would allow for efficient optimization of MD modules.

In order to fill this continuous temperature profile measurement gap in AGMD research, several temperature distribution measurement methods were explored.

Thermocouples provide a good spatial resolution (down to 0.03 mm, Fang and Ward (1999)). However, when physically placed inside the module, they may impede water flow, particularly in laminar flows. Moreover, thermocouples only provide local measures. To obtain a temperature profile perpendicular to the flow, either a moving thermocouple, which complicates module sealing and perturbs the flow, or several thermocouples, further increasing the flow perturbation, are required. Microfluidics approach uses fluorescent dye that emits a wavelength proportional to the temperature (Ross et al., 2001; Sakakibara and Adrian, 1999; Natrajan and Christensen, 2020). However, evaporation of water at the membrane might result in a dye concentration gradient close to the membrane, that may impede the interpretation.

Schlieren method, interferometry and shadowgraphy are optical techniques based on dependency of the liquid refractive index on temperature. Interferometry exploits the phase change of a light ray passing through an inhomogeneous refractive index region to detect temperature gradients. Schlieren method uses the deflection angle of light rays to get the first derivative of the refractive index. Shadowgraphy is based both on the deflection and displacement of the ray, however the observation is more challenging than other techniques (Kroiß et al., 2014) . Interferometry is the most precise method since it delivers the refractive index directly, unlike Schlieren method and shadowgraphy which offer the first and second derivatives respectively. This might introduce errors during data interpretation. Ultimately, interferometry is quite complex and vibrations-sensitive while shadowgraphy is not well adapted to quantitative image interpretation. Thus, the Schlieren method is selected for its simplicity and robustness.

Schlieren method is used both qualitatively and quantitatively in a lot of application domains. It was recently used to observe the flow of an N95 respirator with and without exhalation valve (Staymates, 2020) or supersonic aircrafts in flight (Heineck et al., 2021).

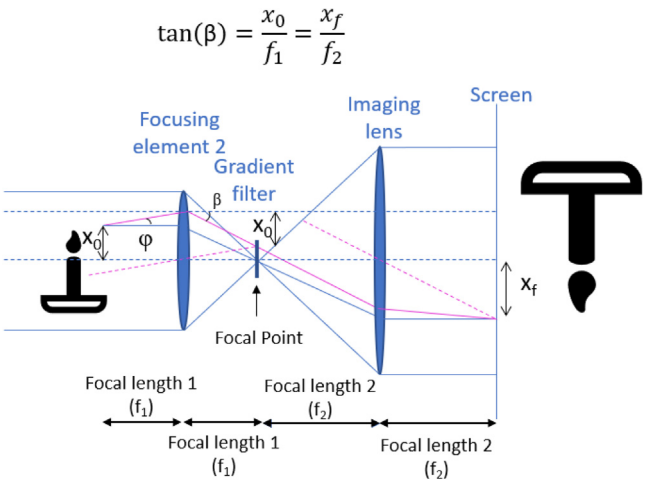

Fig. 1. Path of a ray deflected by a schliere. In purple a deflected ray; in blue the undeflected ray. Whatever the deflection angle experienced by the ray in x_0, its final position on the screen in this specific configuration will always be x_f. (For interpretation of the references to color in this figure legend, the reader is referred to the web version of this article.)

It was also used as a temperature measurement for leader discharge in plasma (Zhao et al., 2019), or as measurement of the human thermal plume flow velocity (Gena et al., 2020).

Hence, in this work the newly developed experimental setup designed to measure temperature distribution inside the hot water channel of a prototypical AGMD module is presented. Along with explaining the operation and chosen measurement method, early measurement results are presented and interpreted.

2. Theory

The Schlieren method uses the fact that light bends as it travels through an inhomogeneous density region.

Deflection angle measurement. In a Schlieren setup a beam of parallel light rays is created and focused at a focal point (see Fig. 1). When crossing an inhomogeneous density region, only the rays not deflected by the medium focus precisely on the focal point while those deflected are slightly shifted.

The light source and the knife or filter lie in a conjugate plane, meaning that what appears in one plane also appears in the other. The test section and the screen as well.

When the object is precisely in the second focusing optical element's focal plane and the screen is precisely in the imaging lens' focal plane, the ray's final position on the screen $x_f = \frac{f_1}{f_2} x_0$ depends only on the initial position x_0, and not the deflection φ (Fig. 1). Thus, regardless of the deflection angle φ, the ray ends up in the proper spot on the screen, and the image displayed on the viewing device in the absence of a filter or knife, is identical to that of the test section except for the magnification factor.

This deflection angle is exploited by placing a filter gradient at the focal point of the focusing element and altering the intensity of this ray without changing its position. The rays' deflections are thus seen as fluctuations in the object picture intensity.

Both knife and gradient filters allow for quantitative Schlieren measurement. The knife method's deflection angle range is restricted by the focal point's diameter (Settles, 2001). If the deflection angle is too large, the deflected ray will be completely blocked and appear dark on the screen regardless of the deflection angle. The gradient filter's disadvantage is that the minimum deflection angle detectable is fixed by the filter characteristics.

Fig. 2 gives an overview of the complete Schlieren setup used in this work.

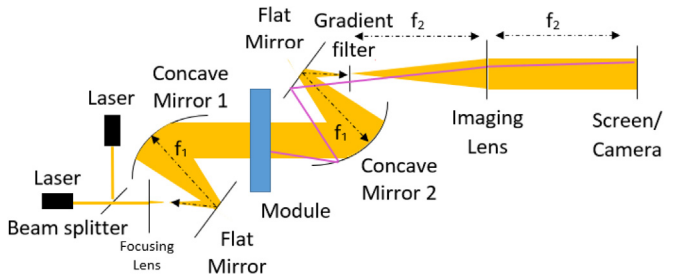

Fig. 2. Sketch of a Z-Schlieren set-up. In purple, a bent ray deflected by the inhomogeneous refractive index medium inside the module, inducing a variation of intensity on the screen.

Linking the deflection angle to the temperature gradient. Deflection angle φ in the experimental AGMD module were verified to be << 1°, hence the wave equation linking the deflection angle to the refractive index n (Eyerer, 2014) takes the form:

$$\varphi = \int_0^l \frac{\ln(n)}{\delta x} dz \tag{1}$$

with l the width of the medium crossed by the ray.

Moreover, according to Snell's law, $n_a \sin(\varphi'') = n_w \sin(\varphi)$, with n_a the refractive index of ambient air and φ the deflection angle in water ray; φ'' the deflection angle of the light ray emerging from the test cell of refractive index n_w. Thus, for small values of φ'' and φ, $\varphi'' \approx \frac{n_w}{n_a} \varphi$, and in Eq. (1):

$$\varphi'' = \frac{n_w}{n_a} \int_0^l \frac{1}{n} \frac{\delta n}{\delta x} dz \tag{2}$$

Since $\frac{1}{n}$ does not change significantly through the test section and since $n_a \approx 1$, the previous equation becomes:

$$\varphi'' = \int_0^l \frac{\delta n}{\delta x} dz \tag{3}$$

Further assuming that the refractive index gradient along a single ray path is constant, and applying a linear interpolation of the curve representing the refractive index as a function of temperature, the previous expression becomes:

$$\varphi'' = l \times a \frac{\delta T}{\delta x} \tag{4}$$

with a the slope of the linear interpolation of n as a function of T (Fig. 22).

Hence the Schlieren approach relates light intensity variations to refractive index gradients, and so to the temperature (and concentration) gradient.

Because the refractive index n is wavelength-dependent, using two wavelengths provides two independent equations in the form of (Eq. (5)), allowing two unknowns to be estimated at the same time — such as temperature and concentration (Panigrahi and Muralidhar, 2012) .

3. Methodology

3.1. Test facility

The test facility is designed to allow adjusting operating parameters like hot and cold water temperatures, feed flow, and evaluate their influence on the process (Fig. 3). It is composed of a desalination module described in 3.3, a pump circulating the fluid, devices to heat and cool the water, and the polarization observation equipment described in 3.2.

A heater and a cooler with PID controller maintain stable temperatures of the hot and cold-water flows. The setup is covered to remove the impact of the ambient light on the optical measurement, and pictures were taken at night to ensure an identical background illumination.

To avoid pump-induced vibrations interfering with the optical setup, the heated tank is elevated and fed by a peristaltic pump. It draws water from an intermediate tank located at the module's altitude, which collects the water exiting the module. This water feed setup produces a smooth gravitational flow with minimal heat losses, thanks to the installed insulation. Two valves situated before and after the module regulate the flow.

Thermocouples (type T) and pressure transducers are used to measure the temperature and pressure before and after the module.

An inspection with an infrared camera revealed that the most significant thermal losses occur in the feeding pipes of the setup. These were insulated accordingly to prevent the water from cooling down. In addition to leading to poorly controlled inlet condition, cold water absorbs more air, which may then be released as bubbles in the pipes and obstruct the flow.

A degassing valve is installed at the upper tank's output to remove accumulated air bubbles that form when the water in the system heats up.

3.2. Optical set-up

3.2.1. Description of the equipment

Light source. A two-wavelengths Schlieren method is set up to investigate the temperature and concentration profiles across the hot water channel of a prototype AGMD module. The chosen wavelengths must be of similar intensity, stable in space, time and spectrum (Eyerer, 2014), and present the broad spectrum range. This work focuses on the application of a green laser with wavelength of 532 nm.

Optics. Two types of Schlieren setups can be used:

- using lens-based setup, requiring a lot of space and susceptible to achromatism
- "Z-shaped" setup using mirrors, resulting in reduced space requirements, but more susceptible to astigmatism

Due to space constraints, the z-shaped set-up was chosen (see Fig. 2).

Two achromatic concave mirrors with a focal length 500 mm and a diameter of 75 mm are used, corresponding to a f-number of at least 6 (6.66, as advised in Settles (2001)) which limits the risk of spherical aberration and astigmatism. An additional imaging lens of focal length 1000 mm provides a 2X magnification. Two flat mirrors are added to the Z's short arms to prevent the beam from interfering with the module's surroundings. In addition, using the symmetrical Z configuration allows for partial compensation for coma aberrations (Settles, 2001). To further reduce coma risks the angle between the Z's arms is kept as low as feasible (0.26 rad = 14.89°) (although still greater than the recommended 5° (Kook et al., 2011)).

Schlieren knife. Because a laser is used as a light source, it focuses to a point at the focal plane, making knife edge calibration unfeasible. Thus, a gradient filter[1] is used. According to the calibration provided calibration curve, the displacement Δx of the light ray

[1] NDL-10C-4, Thorlabs

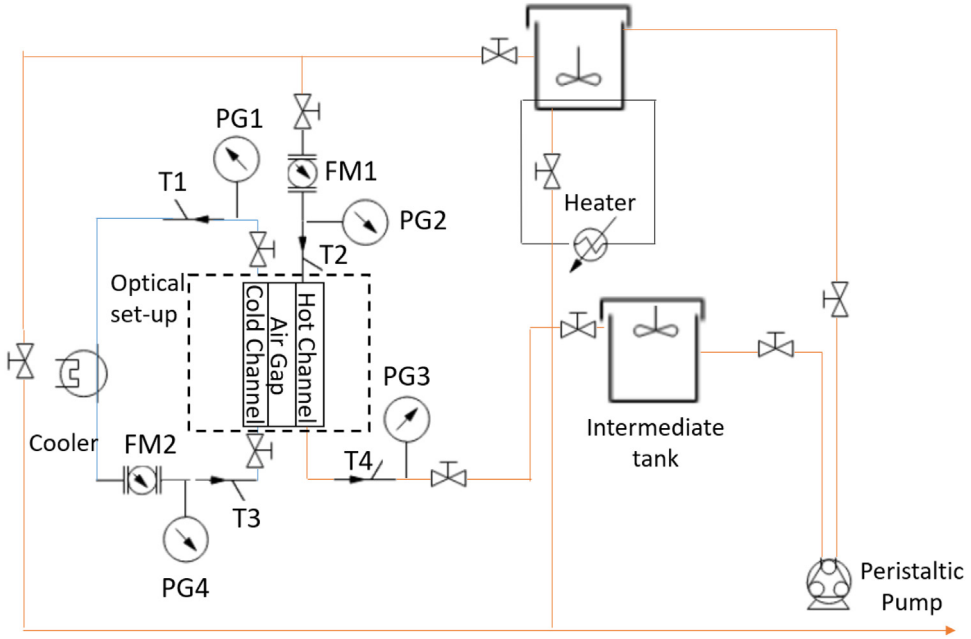

Fig. 3. P&ID Sketch of the set-up with indication of location of thermocouple (T), pressure gauge (PG) and flow meter (FM).

at the focal point occurring due to the presence of a temperature gradient in the test section can be calculated according to:

$$\Delta x = \frac{45}{4} \log_{10}\left(\frac{I_0}{I_\varphi}\right) \tag{5}$$

with I_0 the received intensity at a given image pixel recorded without temperature gradient in the test section, and I_φ the received intensity at the same pixel when a temperature gradient is present in the test section and deflects the light ray by an angle φ (Fig. 19).

Camera. The camera used is a Fujifilm XT-2.

Since the magnification desired in the set-up is 2X, and since the used mirrors' focal length is 500 mm, a 1000 mm external imaging lens is used.

3.2.2. Resolution of the schlieren set-up

As the gradient filter is 50 mm*10 mm, for an equal determination of the temperature variation in both directions, the maximum observable angle is estimated as $\varphi_{max} = atan\left(\frac{\frac{50}{2}}{f_1}\right) = atan\left(\frac{25}{500}\right) = 0.049$ rad. The corresponding angle on the water side is thus $\varphi_{w,max} = asin\left(\frac{n_a}{n_w}\sin(\varphi_{max})\right) = 0.037$ rad.

Following Eq. (4), the maximal temperature gradient observable is thus $\left.\frac{\delta T}{\delta x}\right|_{max} = \frac{\alpha_{w,max}}{L*0.0002} = 18$ °C/mm with L the module length equal to 10 mm.

The resolution can be calculated according to:

$$\left.\frac{\delta n}{\delta x}\right|_{min} = \frac{n_a}{l}\frac{t_0}{f_1}\frac{1}{\frac{dt}{dz}}C_{min} \tag{6}$$

with t the filter's transmission function and C_{min} the minimum resolvable contrast by the imaging device. In this case, the camera, has a C_{min} of 0.4%). Since $\frac{dt}{dz} = -t$, the resolution varies along the filter. At the transparent side, the resolution is about 0.0000004 mm^{-1} (or 0.002 °C/mm) and goes towards 0.004 mm^{-1} (20 °C/mm) at dark border of the filter. Thus, a use of a portion of the filter area on the transparent side complies with the requirements for a two-wavelength Schlieren method.

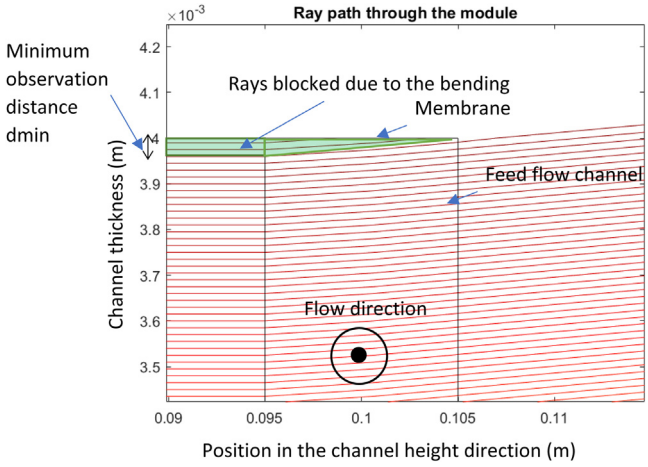

Fig. 4. Deflection of the rays in the Module. The thickness of the channel is marked on Y axis and the channel height on X axis.

3.3. AGMD module

The module's internal dimensions and shape were determined by two main constraints: the capacity to observe the temperature profile near to the membrane, and the ability to maintain a laminar flow in the hot water channel.

Due to the bending of the rays as they pass through the inhomogeneous refractive index gradient media, the closest rays to the membrane are blocked, and the first detectable ray that exits the module, travels at a certain distance from the membrane. A raytracing program has been created to analyze the rays' paths in the module and through the optical setup. It allowed to test variable input parameters such as the temperature gradient profile. Fig. 4 presents an example simulation result.

Clearly the minimum distance at which temperature close to the membrane can be observed is limited by the module's height. Thus, the module should be as small as possible to observe temperatures close to the membrane. Due to construction constraints,

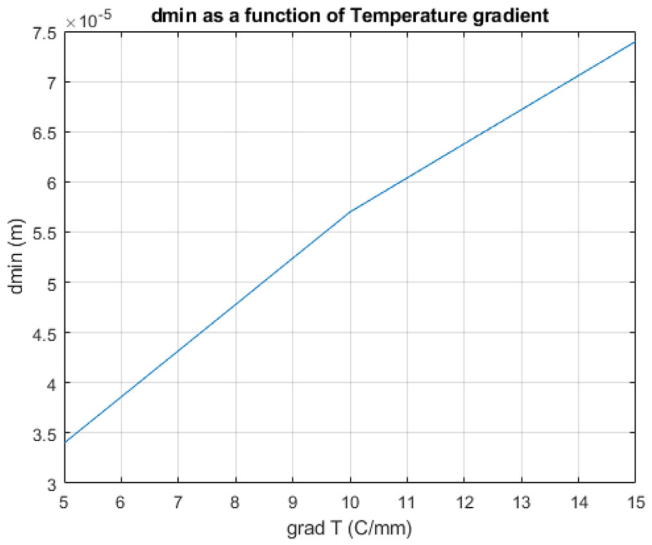

Fig. 5. Minimum observation distance dmin for different temperature gradients at the membrane interface.

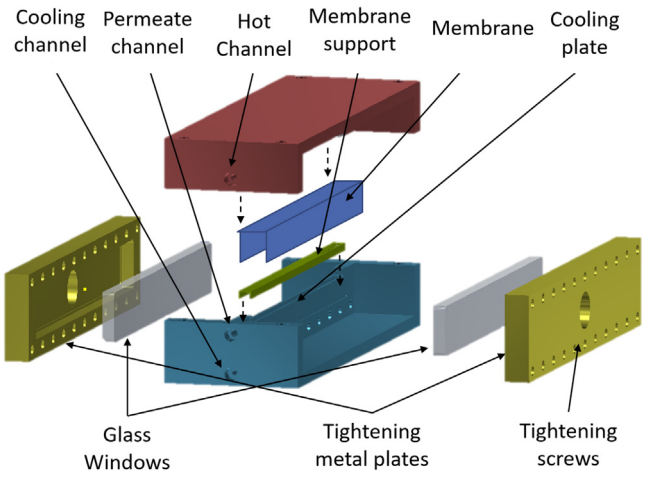

Fig. 6. Exploded drawing of the module.

a minimum height of 10 mm was necessary. The minimum distance from the membrane at which the temperature profile is observable depends on the temperature gradient intensity at the membrane, and represented in Fig. 5.

Taking into account the 10 mm channel height, to ensure a laminar flow with this module height and planned range of mass flows, the thickness of the channel should not exceed 5 mm.

From the measurement perspective, it is desirable to avoid entrance effects and ensure fully developed flow profile in the module. The calculated entrance length of the flow inside a channel of such a geometry was too large to accommodate in the proposed experimental setup. Therefore, a conditioning grid at the entrance has been included (as in Wolf (2014)).

To avoid light rays' obstruction, neither support structure nor a gasket could have been added on the hot water channel side of the. The challenge of ensuring the water tightness of the module has been overcome by wrapping the membrane around the air-gap channel, as proposed in Wolf (2014) . This wrapping prevents the use of O-rings, thus a pliable sealant was used for water tightness.

The prototype is made as a double sandwich structure with horizontal and vertical layers to ensure the water tightness (Fig. 6).

Resin was first selected as a module material for its low heat conductivity. However, due to water tightness issues caused by cracks in the module at operating conditions, a metal prototype was manufactured instead (Fig. 23) with dimensions 35 × 11 × 9 cm. To minimize the resulting heat losses caused by the use of this material, the module is insulated. The overall free membrane surface is $1.15.10^{-3}$ m^2.

Due to water capillary length being very close to the dimensions of the air-gap inlet and outlet ($l_w = 2.7$ mm), the module has to be used vertically to ensure proper condensate drainage and prevent air-gap filling.

The membrane used is a GORETEX sample which was available and selected for its configuration in a rectangular roll, fitting to the module length constraints.

3.4. Temperature profile reconstruction algorithm

For each boundary condition, a picture of the Schlieren image on the screen is taken, and compared to the same picture taken without any temperature variation nor flow. For each pixel, the intensity between the two pictures are compared, and the gradient filter's transmission function allows to determine the displacement Δx along the gradient filter of the ray corresponding to that particular pixel according to Eq. (6) (Fig. 7).

Knowing the second concave mirror' focal length f_1, the apparent deflection angle φ_{app} can be calculated as

$$\varphi_{app} = atan\left(\frac{\Delta x}{f_1}\right) \tag{7}$$

A correction is applied to consider the diffraction occurring in the polycarbonate window as the light beam exits the module, and provides φ_{real}. The temperature variation across the hot water channel is obtained after transforming Eq. (5):

$$\frac{\delta T}{\delta x} = \frac{\varphi_{real}}{l \times a} \tag{8}$$

The images are acquired in JPG format and after loading the data is stored in three tables corresponding to the red, green and blue channels. The green channel is saturated by the laser light. Thus, the blue component of the images is used, as it provides a suitable variation of intensity. In future experiments, a filter could be used in order to dim the intensity reaching the camera and avoid the saturation.

The camera does not respond linearly to the incoming intensity. This response can be found by taking 6 pictures of the same scene with low dynamic range and different exposure times, and use MATLAB's camararesponse function, providing the correlation between the pixel value (intensity) to the log of the incoming intensity (exposure) (Fig. 8)

The inverse curve, providing the log of the incoming intensity as a function of the pixel value, is interpolated thanks to a polynomial p, later on used in the main reconstructing algorithm. Indeed, the algorithm presented in Fig. 7 is concerned with the actual intensity of the light ray striking the camera chip, whereas the camera delivers a pixel value (pix) proportional to the induced electric signal.

The camera is remotely activated to avoid disturbing its position. Due to the vibrations caused by the cooling system, some minor translation between images may happen and has to be quantified. Moreover, it was observed that the membrane interface is not flat, most likely due to the membrane support (see left hand side of Fig. 9(a)).

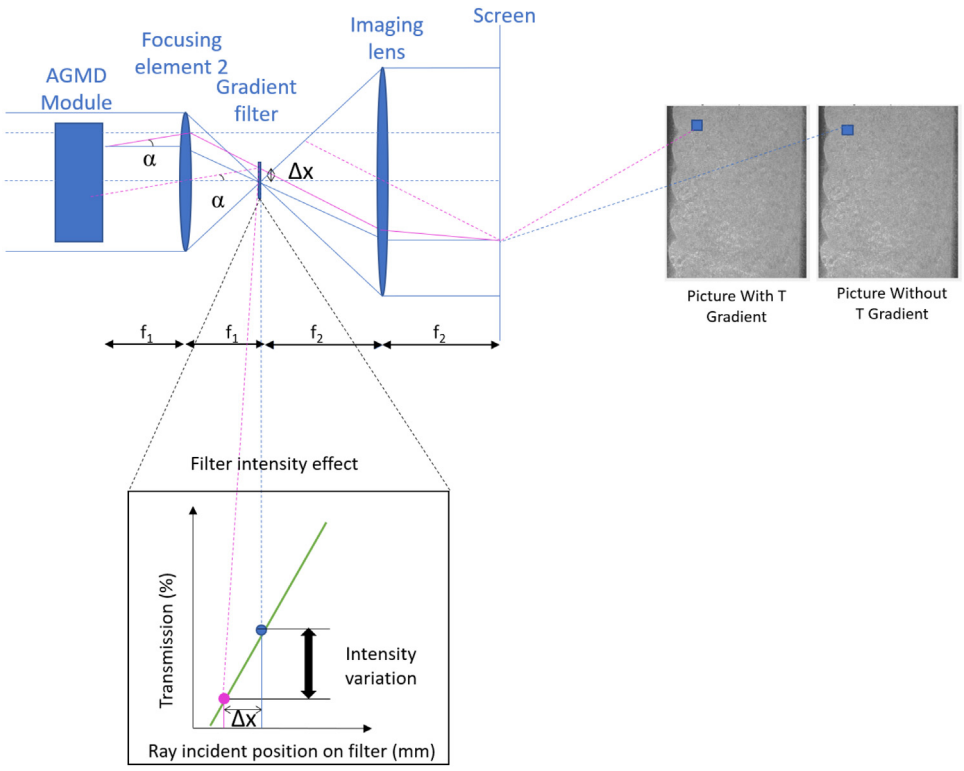

Fig. 7. Reconstruction algorithm. In blue an undisturbed ray, in purple a deflected ray.

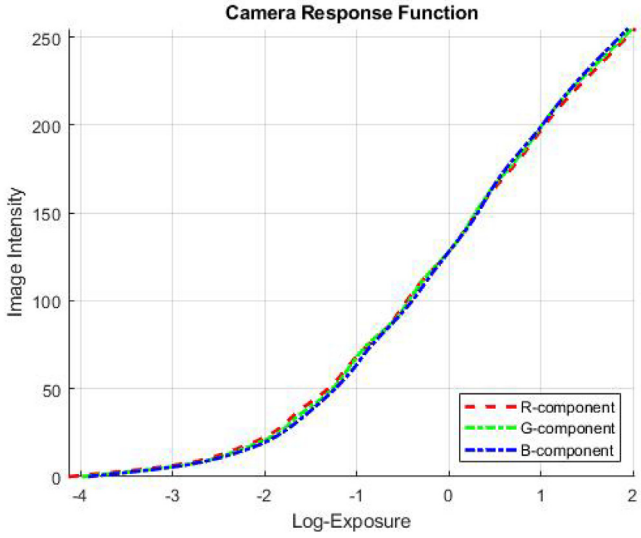

Fig. 8. Estimated Fujifilm XT-2 camera response function.

Hence, a simple algorithm is constructed to determine the translation relative to an image that does not have a temperature gradient. This algorithm calculates a two-dimensional cross-correlation between the pictures. Afterwards, the appropriate translation is applied to the second picture.

To remove the apparent noise on the picture, a low-pass filter is applied to both pictures with a temperature gradient and without.

To identify the membrane interface in the pictures, first a binarization of the image (see Fig. 9(b)) is conducted. Then, the position of the first "light" pixel of each row is recorded, depicted in blue in Fig. 10. Similarly, the opposite wall of the hot water channel is identified as the last pixel which intensity value surpass a given threshold. Finally, a low-pass filter is applied to smooth the obtained curve and approximate the membrane interface (in orange in Fig. 10), and a polynomial fit for the opposite wall. Low pass filtering has been chosen, as the interface is continuous and its position has to change smoothly. Therefore, the observed high-frequency spatial noise in the reconstruction is unphysical and had to be filtered out. As a cut-off spatial frequency value of 0.008 pix^{-1} (or about 0.5 mm) was chosen. This value is in the same range as the distance between the membrane support structure, and corresponds to the expected bumps/ hollows distances.

Then, for each pixel row of the image, starting from the identified membrane interface position, a reconstruction of the temperature profile is attempted using the algorithm depicted in Fig. 7.

On Fig. 10, the membrane appears to be not perfectly vertical, however the tilting angle is very small and will not affect the temperature profile reconstruction.

First, in order to smooth the apparent noise on the raw picture due to light diffraction in the polycarbonate sheet, a low-pass filter is applied (Fig. 11) before converting each row to a temperature profile using Eq. (6).

Due to the very strong and observable heat transfer occurring at the wall side of the module, there is no guarantee that the maximum temperature in the channel corresponds to the inlet temperature. The membrane temperature is therefore arbitrarily set to 0 °C, and rather than the absolute temperatures the differences and slopes of the temperature profiles are considered.

3.5. Precision of the method

There are several sources of error in this experiment:

- due to the position error of the optics

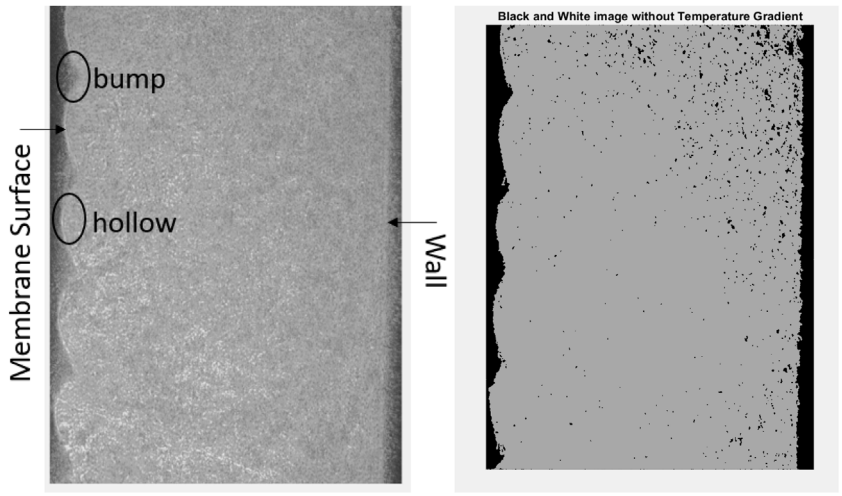

a) Original picture b) Binarized picture

Fig. 9. Schlieren pictures of the hot channel of the module (a) original (b) with binarization treatment. Membrane interface on the left side; hot water channel wall on the right. The water flows from bottom to the top.

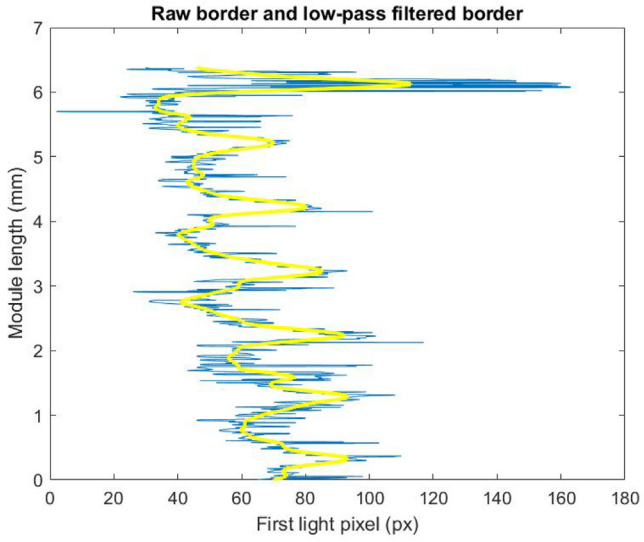

Fig. 10. Index of the first "light" pixel in each image row, representing the membrane interface, raw data in blue, filtered data in yellow. (For interpretation of the references to color in this figure legend, the reader is referred to the web version of this article.)

- the image capture system
- the reconstruction algorithm (Section 3.4).

All of them are explored in the next sections.

3.5.1. Errors from the position error of the optics

All the optical equipment is located on a micrometric table, enabling their positioning at the precision of ±0.5 mm.

Spatial Resolution.

The position error Δx_{mirror} of the mirror induces an enlargement of the image on the screen by a factor of $e_{mirror} = \frac{D}{2}(1 + (L - 2fl)\frac{\Delta x}{fl})\frac{fl}{fl2}$, where D is the original beam diameter, L the distance between the two mirrors, and fl and fl2 the focal length of the mirrors and the imaging lens respectively. For $\Delta x_{mirror} =$ 0.5 mm, the enlargement factor is $e_{mirror} = 1.0005$.

A position error Δx_{screen} of the screen also results in a deformation of the image on the screen. This error is hard to evaluate as it depends on the angle of the deflected rays. Taking a maximum deflection of roughly 5 mm at the focal point for the ray coming from the furthest corner of the channel ($tan(\varphi_{max}) = \frac{H+5mm}{fl}$), an overall maximum deformation of $e_{screen,max} = \Delta x tan(\varphi_{max})$ is obtained. For a position error of $\Delta x_{screen} = 0.5$ mm, the error is 0.0025 mm.

Intensity resolution. If the gradient filter is moved by Δx_{filter}, it results in a change in the intensity of variation of $e_{filter} = 10^{-\frac{45}{4}tan(\varphi)\Delta x}$ for a ray of deflection angle φ. For $\Delta x_{filter} = 0.5$ mm, the resulting coefficient in intensity variation is $e_{filter} = 0.99979 I_0$.

3.5.2. Errors from the image capture system

Spatial resolution. As the pixel size of the camera sensor is 3.9 μm and the magnification coefficient of the optical set-up is 2, the theoretical spatial resolution of the described setup is $e_{pix} = 1.95$ μm.

Intensity resolution. The intensity on the camera chip is registered in an 8 bit format, scaled to [0, 1] interval during processing. Therefore, the pixel values are discrete values $e_{chip} = \pm\frac{1}{256} \sim 0.0039$.

The camera also produces noise, and the signal (S)-to-noise (N) ratio for Fujifilm XT-2 is estimated at 40 dB up to ISO 400 (Igual, 2019). Therefore, the error introduced into intensity measurements $e_{camera} = 10^{-4} pix$.

3.5.3. Errors from the reconstruction algorithm

Spatial Resolution. As the position of the membrane is not identifiable to the nearest pixel, the accuracy range of the membrane determination pixels is in this configuration, $e_{mem} \approx 0.78 pix$ (see Fig. 12), e_{mem} is the average distance between the orange and purple curves defining the 95% confidence interval).

Intensity resolution. A 95% confidence interval ΔI is calculated for the filtering of the intensity profile for each pixel line of the picture, which is spread all along the calculations.

Overall, by differentiating the combination of Eqs. (6), (8) and (9) the impact of the filtering uncertainty ΔI on the temperature

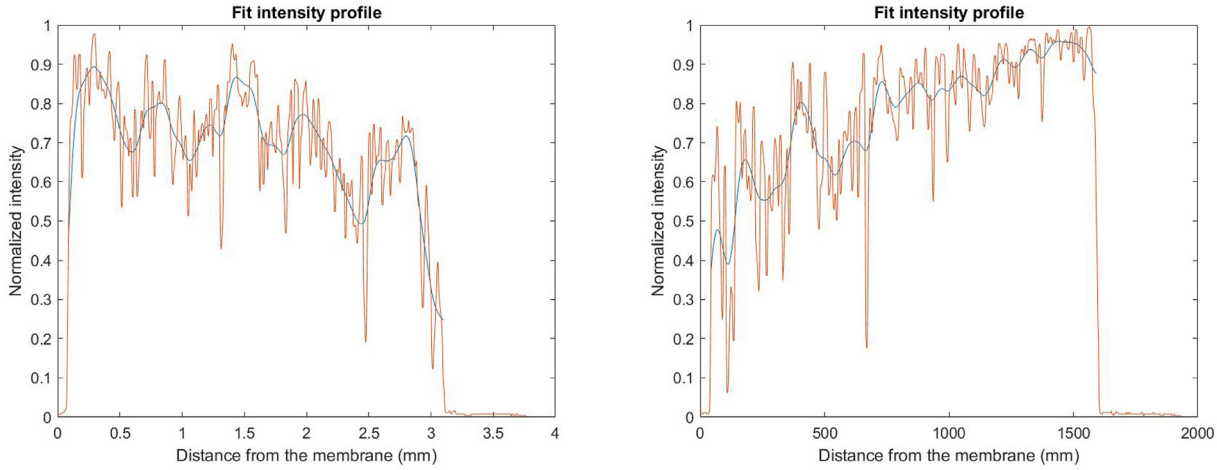

a) With a Temperature gradient of about 13°C/m

b) without a Temperature gradient

Fig. 11. Interpolation of the intensity profile — raw data in red, low-pass filtered in blue. (For interpretation of the references to color in this figure legend, the reader is referred to the web version of this article.)

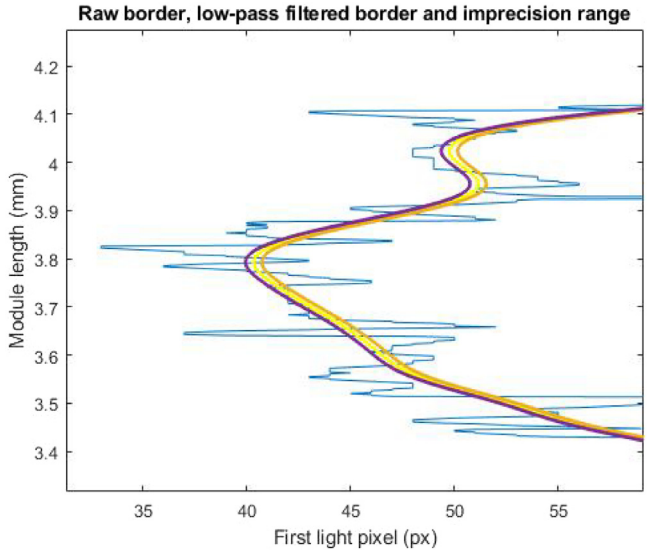

Fig. 12. Evaluation of the pixel imprecision of the membrane interface position determination. In blue the raw data; in yellow the filtered data; in purple and orange the confidence interval determining the 99% confidence interval. (For interpretation of the references to color in this figure legend, the reader is referred to the web version of this article.)

gradient can be calculated as follows:

$$\frac{\Delta dT}{\Delta I} = \frac{45}{4fl_1}\frac{1}{0.0002 * L}\frac{p'(I_0) - p'(I)}{1 + \left(\frac{45}{4fl_1}(p(I_0) - p(I))\right)^2}\frac{n_q}{n_w} \times \frac{cos\left(atan\left(\frac{45}{4fl_1}(p(I_0) - p(I))\right)\right)}{\sqrt{1 - \left(\frac{n_q}{n_w}sin\left(atan\left(\frac{45}{4fl_1}(p(I_0) - p(I))\right)\right)\right)^2}} \quad (9)$$

with p the camera response curve, L the module length, I_0 the intensity after the filter without temperature gradient and I with.

The intensity error source is identified as the polycarbonate sheet as can be seen in Fig. 13, showing diffraction caused by this material.

3.5.4. Errors' summary

As a conclusion, the method's spatial resolution is on the order of magnitude of $resol_{spatial} = pixsize \pm pixsize\left(1 - \frac{1}{e_{mirror}}\right) = 1.95 \pm 9.7 * 10^{-4}$ µm while the precision is on the order of magnitude of $exact_{spatial} = (1 - e_{mirror}) * e_{screen,max} = (1 - 1.0005) * 0.0025$ mm $= 1.25 * 10^{-6}$ mm. The method's intensity resolution is on the order of magnitude of $resol_{spatial} = 0.0039 * p'\left(p^{-1}(I_0)\right)$ while the precision is on the order of magnitude of $exact_{spatial} = I_0 \pm (1 - 0.99979) * 10^{-4} p^{-1}(I_0)$.

4. Results

Despite insulation, unavoidable temperature variations along the pipe circuit of the experiment occur, resulting in air bubbles in the pipes, reducing the flow during the course of measurements. Thus, short time (<30 min) measurements are performed. The corresponding calculated Reynolds numbers for the presented results range from 2524 and 3674. The temperature and velocity ranges are consistent with those seen in AGMD studies (Xu et al., 2016a; Summers and Lienhard, 2013).

The following figure (Fig. 14) shows twenty reconstructed temperature profiles around one of the hollows of the membrane for the same inlet velocity ($V_{in} \sim 0.2$ m/s), and hot water temperature ($T_{hot} \sim 74$ °C), measured at different dates (see Figs. 16 and 17).

Comparing the two measurements, small variability of the signal persists, but overall the methods has been proved to be well-reproducible.

Each curve represents the reconstructed temperature gradient at a given row. Moving from red to blue, the curves were calculated for pixel rows located upstream to downstream around a single hollow.

In all cases, two temperature boundary layers can be observed, one at the membrane (left side) and one on the opposite wall (right side), owing to the module material's high heat transfer coefficient. Optimizing module's insulation could prevent the secondary gradient from appearing due to heat losses at the wall side.

Fig. 15 shows the impact of the inlet temperature on the temperature profile. Twenty temperature profiles around the same hollow are shown at an inlet velocity of about $V_{in} \sim 0.18$ m/s, for two different hot water temperatures.

Fig. 13. Picture of the laser light with the polycarbonate sheet protection (left) and without (right).

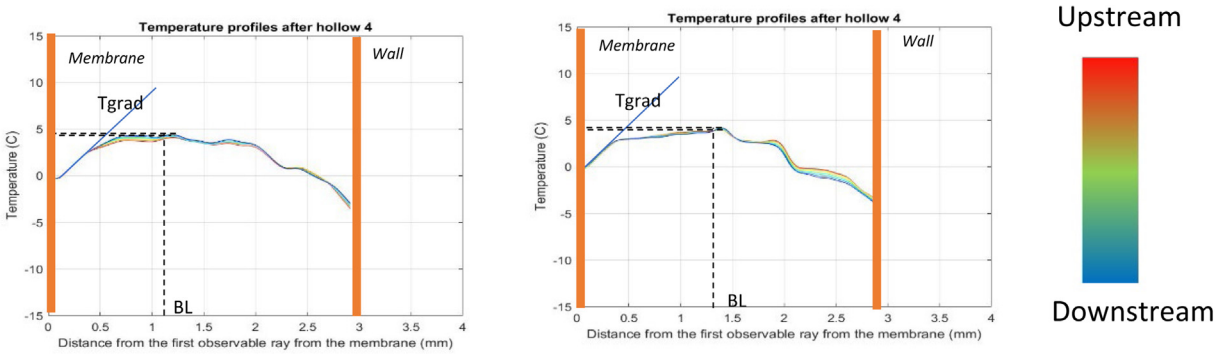

Fig. 14. Reconstruction of the temperature profile for 20 pixel rows around one of the hollows (4) of the membrane for $V_{in} \sim 0.2$ m/s and $T_{\text{hot}} = 74°\text{C}$ measured at different dates (left and right). Temperature gradient at the membrane marked in blue Tgrad and boundary layer with black dashed line BL. (For interpretation of the references to color in this figure legend, the reader is referred to the web version of this article.)

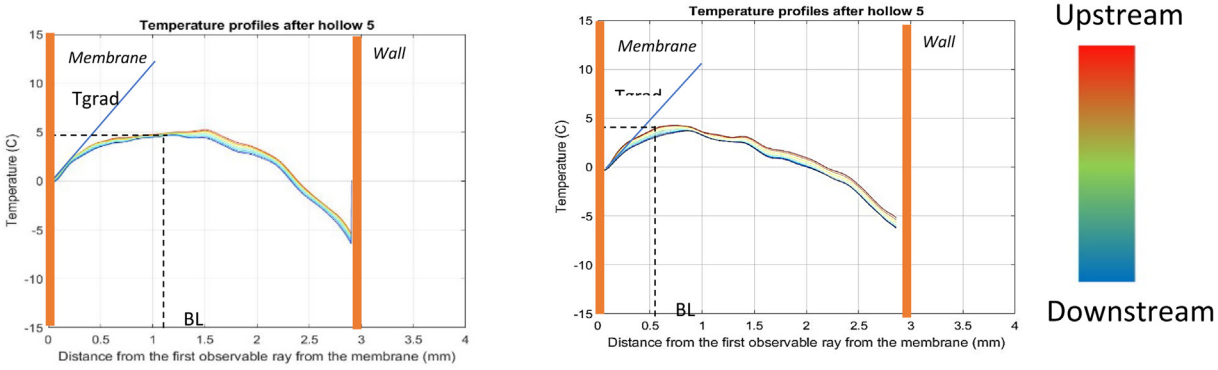

Fig. 15. Reconstruction of the temperature profile for 20 pixel rows around one of the hollows (4) of the membrane for $V_{in} \sim 0.2$ m/s and $T_{\text{hot}} = 73°\text{C}$ (left) and $T_{\text{hot}} = 60°\text{C}$ (right).

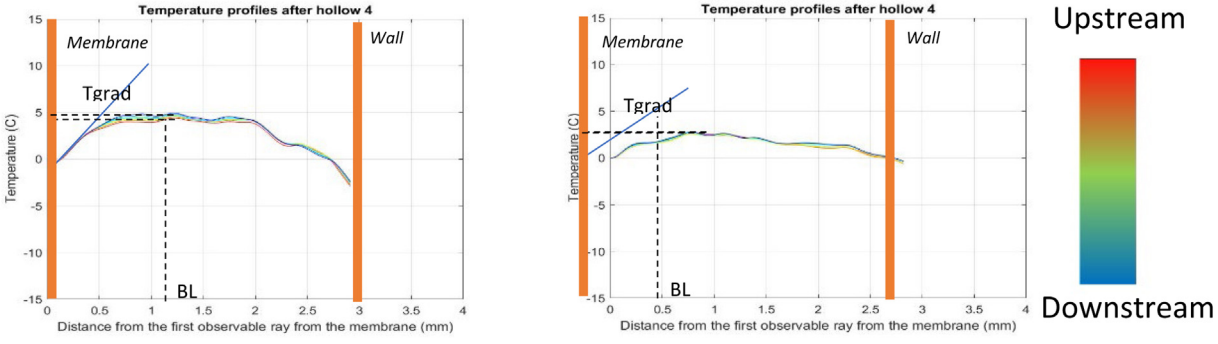

Fig. 16. Reconstruction of the temperature profile for 20 pixel rows around one of the hollows (6) of the membrane for $T_{\text{hot}} = 74°\text{C}$ and $V_{in} \sim 0.18$ m/s and $V_{in} \sim 0.225$ m/s from left to right.

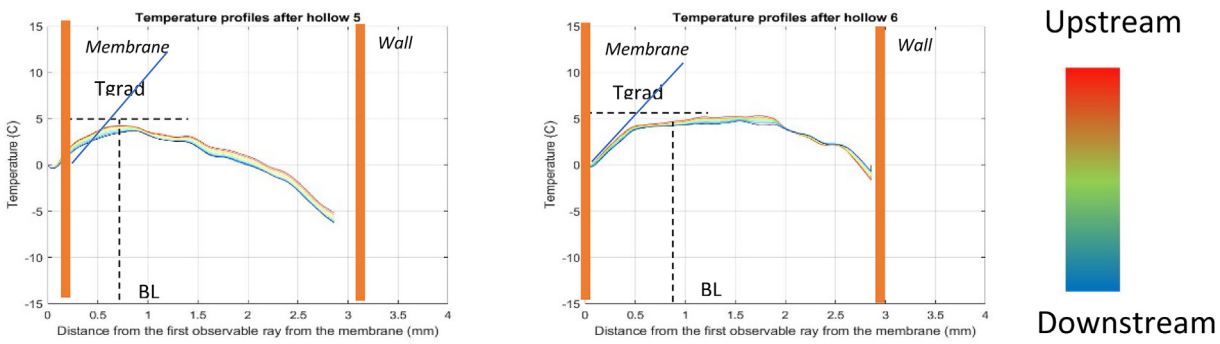

Fig. 17. Reconstruction of the temperature profile for 20 pixel rows around two different "hollows" (6 and 7) of the membrane for $T_{\text{hot}} = 74°\text{C}$ and $V_{in} \sim 0.18$ m/s.

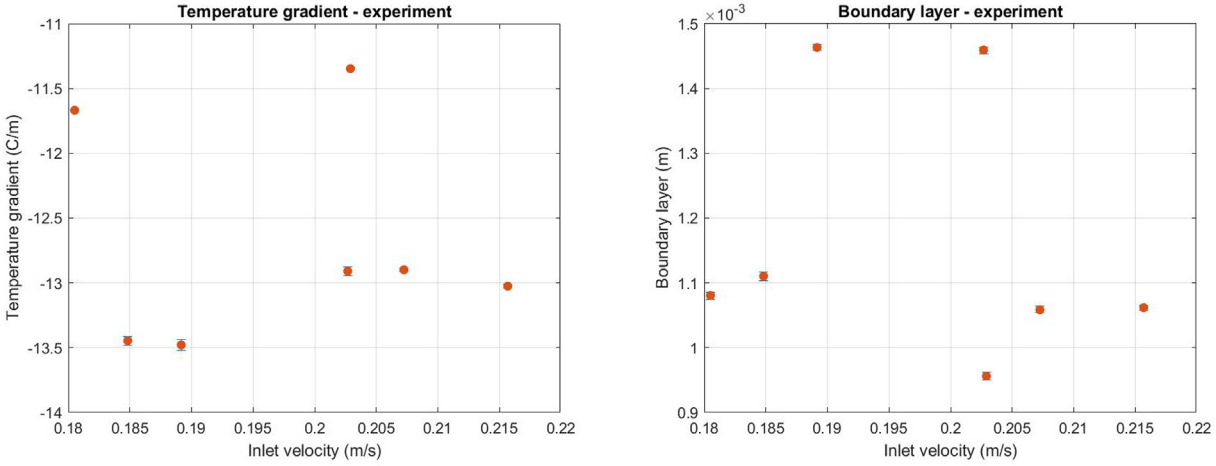

Fig. 18. Averaged temperature gradient (left) and boundary layer thickness (right) at different inlet temperatures versus the inlet velocity V_{in}.

The following plot (Fig. 18) shows the impact of the inlet flow velocity on the temperature profile for two different inlet velocities. $V_{in} \sim 0.18$ m/s, and $V_{in} \sim 0.225$ m/s.

A change in the temperature profile also seems to develop along the membrane, as shown in Fig. 19 representing the temperature profiles at two different hollows of the membrane for the same measurement.

The results are summarized in Fig. 18 and Fig. 19. The boundary layer thickness is calculated assuming the highest temperature in the profile is the bulk temperature. The temperature gradient is the slope of the temperature profile at the membrane interface. Both boundary layer thickness and the value of the temperature gradient at the membrane side are averaged over the whole module length versus the inlet velocity (V_{in}).

Fig. 19 represents the same results versus the inlet temperature along with a linear interpolation of the data and the corresponding R^2 coefficient. The color represents the variance in inlet velocity according to the color scale on the left.

According to the MATLAB ray-tracing simulation, for these temperature gradients, the first observable exiting ray is located at $6.8 \cdot 10^{-5}$ m from the membrane as shown in Fig. 20, which is already smaller than the spatial resolution of the camera.

5. Discussion

5.1. Discussion of the results

As expected, the temperature profile at the membrane interface for a higher inlet hot water temperature is steeper than for a lower hot water temperature==. Indeed, a correlation between temperature gradient at the membrane interface and inlet hot temperature can be observed, as shown in Fig. 19.

The heat loss at the wall side appears to change between different measurements taken at the same operating conditions. This might be due to the ambient temperature of the room, which was not monitored.

No clear dependency of the temperature gradient to the inlet velocity has been identified (Fig. 18).

Alklaibi (2005) investigated numerically the boundary layer thickness of an air-gap membrane distillation device. The hot channel and air-gap thicknesses are 2 mm, the hot inlet temperature is 70 °C and the cold inlet temperature is 20 °C. The resulting temperature gradient at the membrane interface is about 0.075 times the temperature difference between hot and cold inlets temperatures (50 °C), on a distance of about 0.2 times the hot channel thickness, or about 9.37 °C/mm. The boundary layer thickness is about between 0.4 and 0.8 (depending on the location along the channel) times the hot channel thickness, or between 0.0008 m and 0.0016 m. The experimental results presented in this work are coherent with the numerical results from Alklaibi (2005), the larger temperature gradient found in this work could be explained by the lower cold inlet temperature (15 °C).

As can be seen in this study, the temperature gradient at the membrane interface appears to be constant along the hot water channel, which supports the averaging of the temperature gradients performed in this study.

However, the boundary layer thickness does not present any relevant dependency, neither on the inlet velocity nor the hot feed temperature (Fig. 19) in the available data.

A comparison with theoretical boundary layers thicknesses is conducted to validate of the experimental results.

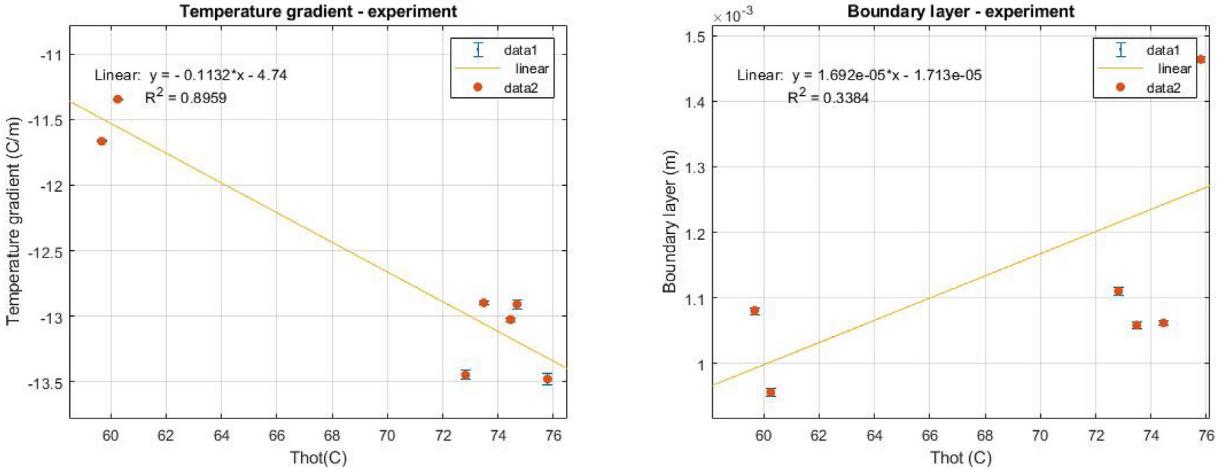

Fig. 19. Averaged temperature gradient (left) and boundary layer thickness (right) for different inlet temperatures and flows represented versus inlet hot temperature T_{hot}.

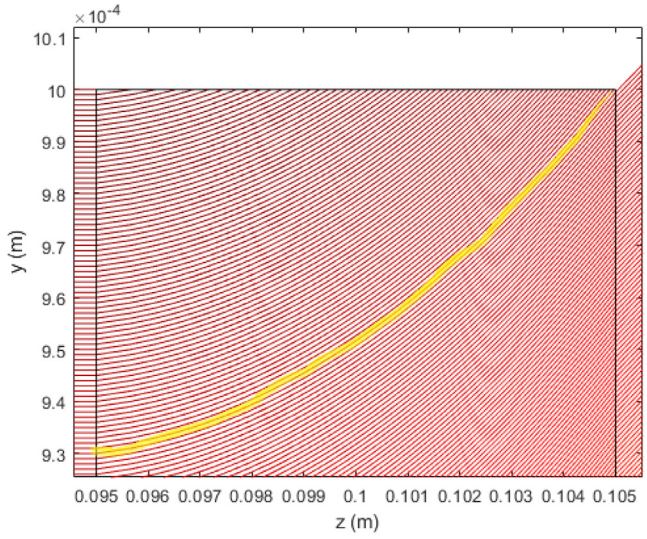

Fig. 20. First observable ray for temperature gradients of 13 C/m.

For laminar flows the thermal boundary layer is given by the Prandtl boundary layer theory:

$$BL_{Pr} = 5\sqrt{\frac{\nu x}{U_0}}Pr^{-\frac{1}{3}} \tag{10}$$

with U_0 the bulk velocity, x the position along the channel length, ν the kinematic viscosity and Pr the Prandtl number.

For turbulent flows, the thermal boundary layer is equal to the turbulent velocity boundary layer thickness:

$$BL_{turb} = \frac{0.37x}{Re_x^{\frac{1}{5}}} \tag{11}$$

with $Re_x = \frac{U_0 x}{\nu}$.

As the Reynolds numbers of the experiment conditions are in the transition zone, both formulas have been used, Fig. 21. This unstable flow regime is a result of the heat losses present in the current configuration. In fact, due to the heat losses, the flow cannot be too low, or greater inlet temperatures cannot be achieved. In addition, because of the gravity feed, the greatest velocity that may be reached is constrained by the height of the water in the water tank and the height of the tank required to compensate for the pressure drop in the remainder of the pipe system. Consequently, in order to maintain a consistent flow and temperature during the measurement, the minimum and maximum achievable flows are constrained.

The measured boundary layers have the same orders of magnitude, but no agreement is found, and the experimentally determined boundary layer thicknesses are smaller than any of the theoretically calculated boundary layer thicknesses. The reason for this discrepancy might be attributed to several factors. Being in the flow transition area might render the different theories inapplicable to these experiments. According to Schlichting and Gersten (2017), the transition zone occurs at Reynolds numbers of about 2300 occurs at a length equivalent to thousands pipe diameter downstream. This appears to validate the results: the measured boundary layers are most likely still laminar and not yet fully developed, hence the smaller values obtained experimentally compared to the theoretical ones.

The similar phenomenon is observed in the Alklaibi paper (Alklaibi, 2005), where the boundary layer thickness increases downstream the hot channel.

Heat losses on the wall side may also affect the thickness of the boundary layer: indeed, the bulk temperature in the absence of this heat loss may be higher than the current observable temperature, implying that the temperature boundary layer could be larger in the absence of this temperature gradient.

Another hypothesis is that the roughness of the membrane impacts the turbulence of the flow and renders the Reynolds number not representative.

Overall, the obtained experimental results show that the constructed experimental setup is capable of high spatial resolution measurements of temperature gradient in AGMD hot water channel. The challenge of acquiring data extremely close to the membrane (<0.2 mm) remains, but the reconstructed temperature polarization has shown that the thermal boundary layer extends beyond this region and could have been accurately captured.

A number of parameters negatively impacting the measurement resolution has been identified. The setup could be improved by using high quality glass instead of polycarbonate sheets, limiting the observed noise in intensity data. A filter can be introduced to reduce the intensity reaching the camera chip lowering the risk of saturation and enabling use of additional data channels.

Insulation of the test module should be improved, so that the secondary temperature gradient developing at the wall opposite of the membrane is eliminated. The structural support of the membrane should be redesigned, to avoid the formation of the

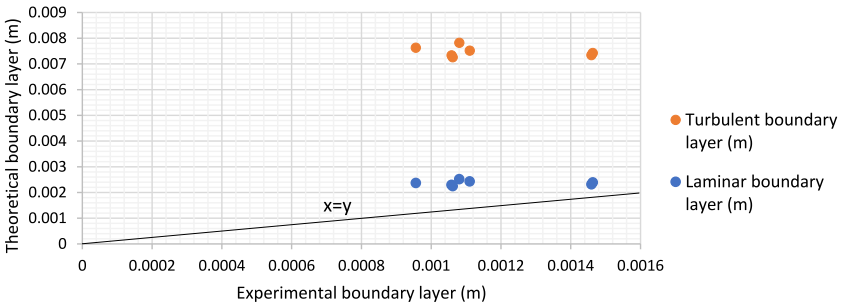

Fig. 21. Laminar and turbulent boundary layer thickness as a function of the experimentally measured boundary layer.

bumps and hollows, which presence adds a layer of complexity to data interpretation. Similarly, effort should be extended to further insulate the optical components and the module from any source of vibration, eliminating the need for image-to-image translation correction step.

Finally, analysis using RAW files instead of JPG should be investigated, to remove and in-camera processing of the data.

A straightforward extension of this work is an addition of a secondary light source. In this way, concentration and temperature profiles could be evaluated at the same time.

6. Conclusion

MD, and among its various configurations AGMD in particular, are a promising response to the incoming global freshwater shortages. With its main limiting parameter preventing widespread adoption being the output flow, this article proposed an observation tool allowing in-depth investigation of module operation.

A test bench allowing the observation of a continuous temperature profile in the hot water channel of an AGMD module has been developed and assembled. The collected data can be further used in order to analyze and potentially optimize the heat transfer in the module. Evaporation process would be thus increased, improving the output flow and the relevance of AGMD for practical applications. In addition to the measurement setup, a prototypical AGMD module is also designed, allowing observation close (∼0.07 mm) to the membrane, both in laminar and turbulent conditions. In further experiments, the module air-gap could also be filled with different materials, extending the setup relevance from AGMD to Material Gap Membrane Distillation MGMD (Abu-Zeid et al., 2020; Cheng et al., 2018) and Conductive Gap Membrane Distillation CGMD (Swaminathan et al., 2015) .

The presented reconstruction algorithm has been shown to successfully process the recorded Schlieren pictures, and provide accurate temperature profiles.

Overall, the proposed observation method providing a continuous temperature profile perpendicular to the hot water channel and close to the membrane is clearly visualizing the impact of operating conditions and evolution of the profile along the channel length. It allows the determination of both a temperature gradient at the membrane, and a boundary layer thickness in the hot water channel.

In further steps, the measurement setup will be used to investigate a range of operating conditions, creating a database of MD temperature distributions.

This experimental data will be used for the validation of numerical simulations, allowing for the evaluation of spacers impact on the output flow and energy efficiency of the AGMD.

In summary, the experimental setup allows to observe temperature gradients up to 18 °C/mm^{-1}, with a resolution as low as 0.002 °C/mm, and the theoretical spatial resolution is of 1.95 μm

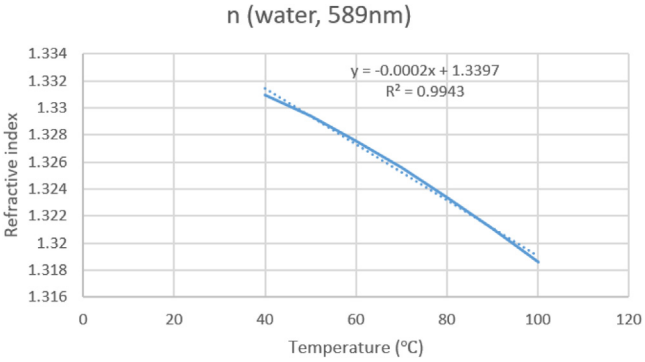

Fig. 22. Variation of the water refractive index with temperature.

Table 1
Equipment details.

Name	Quantity	Brand	Description
Heater	1	Julabo	SL with circulating fluid H20S
Cooler	1	Julabo	F32
Laser 532 nm	1	Thorlabs	CPS532
Gradient filter	1	Thorlabs	NDL-10C-4
Concave mirrors	2	Thorlabs	CM750-500-P01
Imaging lens	1	Thorlabs	ACT508-1000-A
Flat mirrors	2	Thorlabs	
Micrometric table	4	Thorlabs	PT1B

$\pm 9.7 * 10^{-4}$ μm. The membrane location is known with a precision of ±0.78 pixels, which translates to ±3 μm.

Improvements of the observation method could include the manufacture of a test module allowing for simultaneous observation of hot water channel and air-gap temperature gradients.

7. Supplementary information

See Table 1.

Nomenclature

GORGain Output ratio
m_d evaporated mass
h_{fg} specific evaporation enthalpy
Q_{in} heat brought to the system
x_0 initial position of the ray on the object
x_f final position of the ray on the screen
f_1 focal length of the focusing elements
f_2 focal length of the imaging lens
φ ray deflection angle
φ'' angle of the light ray emerging from the test cell
φ_{app} apparent deflection angle
φ_{real} real deflection angle

Fig. 23. Pictures of the module (splitted parts, details of the membrane mounting, internal assembly of the module).

n water refractive index
n_a refractive index of ambient air
l width of the medium crossed by the ray
a slope of the linear interpolation of n as a function of T
Δx displacement of the light ray at the focal point
I_0 received intensity at a given image pixel recorded without temperature gradient in the test section
I_φ received intensity at the same pixel when a temperature gradient is present in the test section
φ_{max} maximum observable angle
$\varphi_{w,max}$ maximum observable angle
t filter's transmission function
C_{min} the minimum resolvable contrast by the imaging device
pix pixel value recorded by the camera

p polynomial interpolation of the inverse of the camera response function
p^{-1} polynomial interpolation of the camera response function
p' first derivative of the polynomial interpolation of the inverse of the camera response function
V_{in} inlet velocity
T_{hot} inlet hot water temperature
BL_{Pr} laminar theoretical thermal boundary layer thickness
BL_{turb} laminar theoretical thermal boundary layer thickness
dmin minimum observation distance from the membrane

CRediT authorship contribution statement

Marie-Alix Dalle: Methodology, Software, Validation, Formal analysis, Investigation, Writing – original draft, Writing – review & editing. **Filip Janasz:** Data curation, Writing – review & editing, Visualization. **Stephen Leyer:** Project administration, Term, Conceptualization, Resources, Writing – review & editing, Supervision.

Declaration of competing interest

The authors declare that they have no known competing financial interests or personal relationships that could have appeared to influence the work reported in this paper.

Data availability

Data will be made available on request.

References

Abu-Zeid, M.A.E.-R., Lu, X., Zhang, S., 2020. Enhancement of the air gap membrane distillation system performance by using the water gap module. Water Supply 20, 2884–2902.

Alkhudhiri, A., Darwish, N., Hilal, N., 2012. Membrane distillation: A comprehensive review. Desalination 287, 2–18.

Alklaibi, N.L.A.M., 2005. Transport analysis of air-gap membrane distillation. J. Membr. Sci..

Alsalhy, Q.F., Ibrahim, S.S., Hashim, F.A., 2013. Experimental and theoretical investigation of air gap membrane distillation process for water desalination. Chem. Eng. Res. Des..

Banat, F.A., Simandl, J., 1994. Theoretical and experimental study in membrane distillation. Desalination 95, 39–52.

Bandelier, P., 2016. Le Dessalement d'eau de mer et des eaux saumâtres.

Cheng, L., Zhao Li, Y., Li, W., Wang, F., 2018. Comparative study of air gap and permeate gap membrane distillation using internal heat recovery hollow fiber membrane module. Desalination.

Chipman, K., 2020. California water futures begin trading amid fear of scarcity.

CNRS, 2013. Découvrir l'eau.

Criscuoli, A., 2016. Improvement of the membrane distillation performance through the integration of different configurations. Chem. Eng. Res. Des..

Eyerer, 2014. Experimental investigation of boundary layers in membrane desalination using quantitative two-wavelengths schlieren.

Fang, G., Ward, C.A., 1999. Temperature measured close to the interface of an evaporating liquid. Phys. Rev. E 59, 417–428.

Gena, A.W., Voelker, C., Settles, G.S., 2020. Qualitative and quantitative schlieren optical measurement of the human thermal plume. Indoor Air.

He Li, Q., Geng, H., Zhang, C., Wang, J., Chang, H., 2014. Modeling and optimization of air gap membrane distillation system for desalination. Desalination.

Heineck, J.T., Banks, D.W., Smith, N.T., Schairer S. Bean, E.T., Robillos, T., 2021. Background-oriented schlieren imaging of supersonic aircraft in flight. AIAA J. 59, 11–21.

Igual, J., 2019. Photographic noise performance measures based on RAW files analysis of consumer cameras. Electronics 8, 1284.

Janajreh, I., Suwwan, D., Hashaikeh, R., 2017. Assessment of direct contact membrane distillation under different configurations, velocities and membrane properties. Appl. Energy 185, 2058–2073.

Kook, S., Le, M.K., Padala, S., Hawkes, E.R., 2011. Z-type schlieren setup and its application to high-speed imaging of gasoline sprays. SAE Tech. Pap. 2011, 01–1981.

Kroiß, A., Eyerer, S., Kuczaty, J., Ties, C., Wolf, S., Präbst, A., Spinnler, M., Sattelmayer, T., 2014. Optical methods for simultaneous measurement of temperature and concentration polarization.

Kurokawa, H., Kuroda, O., Takahashi, S., Ebara, K., 1990. Vapor permeate characteristics of membrane distillation. Sep. Sci. Technol. 25, 1349–1359.

Lawson, K.W., Lyold, D.R., 1997. Review membrane destillation. J. Membr. Sci. 124.

Liu, G.L., Zhu, C., Cheung, C.S., Leung, C.W., 1998. Theoretical and experimental studies on air gap membrane distillation. Heat Mass Transf. 34, 329–335.

Mokhtar, I.E., Boubakri, A., Bouguecha, S.A.T., Hafiane, A., 2019. Modeling and experimental study of air gap membrane distillation unit: Application for seawater desalination. Desalin. Water Treat..

Natrajan, V.K., Christensen, K.T., 2020. Development of fluorescent thermometry methods for microfluidic systems. Mater. Sci. 13.

Panigrahi, P.K., Muralidhar, K., 2012. Schlieren and Shadowgraph Methods in Heat and Mass Transfer. Springer New York, New, York.

Persad, A., 2014. Statistical rate theory expression for energy transported during evaporation.

Ross, D., Gaitan, M., Locascio, L.E., 2001. Temperature measurement in microfluidic systems using a temperature-dependent fluorescent dye. Anal. Chem. 73, 4117–4123.

Saffarini, R.B., Summers, E.K., Arafat, H.A., J. H. Lienhard, V., 2012. Technical evaluation of stand-alone solar powered membrane distillation systems. Desalination 286, 332–341.

Sakakibara, J., Adrian, R.J., 1999. Whole field measurement of temperature in water using two-color laser induced fluorescence. Exp. Fluids 26, 7–15.

Schlichting, Hermann (Deceased), Gersten, Klaus, 2017. Boundary-Layer Theory, Ninth Edition Springer.

Settles, G.S., 2001. Schlieren and Shadowgraph Techniques. Springer Berlin Heidelberg, Berlin, Heidelberg.

Staymates, M., 2020. Flow visualization of an N95 respirator with and without an exhalation valve using schlieren imaging and light scattering. Phys. Fluids 32, 111703.

Suleman, M., Asif, M., Jamal, S.A., 2021. Temperature and concentration polarization in membrane distillation: A technical review. Desalin. Water Treat..

Summers, E.K., Arafat, H.A., Lienhard, J.H., 2012. Energy efficiency comparison of single-stage membrane distillation (MD) desalination cycles in different configurations. Desalination 290, 54–66.

Summers, E.K., Lienhard, J.H., 2013. Experimental study of thermal performance in air gap membrane distillation systems, including the direct solar heating of membranes. Desalination 330, 100–111.

Swaminathan, J., CHung, H.W., Warsinger, D.M., Al-Arzooqi, F., Arafat, H.A., John H. Lienhard, V., 2015. Energy efficiency of permeate gap and novel conductive gap membrane distillation. J. Membr. Sci..

Tamburini, A., Cipollina, A., Al-Sharif, S., Albeirutty, M., Gurreri, L., Micale, G., Ciofalo, M., 2015. Assessment of temperature polarization in membrane distillation channels by liquid crystal thermography. Desalin. Water Treat. 55, 2747–2765.

Wolf, 2014. Implementation of an optical measuring system for investigation of concentration boundary layers in membrane desalination.

Xu, J., Singh, Y.B., Amy, G.L., Ghaffour, N., 2016a. Effect of operating parameters and membrane characteristics on air gap membrane distillation performance for the treatment of highly saline water. J. Membr. Sci..

Zhao, X., Liu, L., Yue, Y., He, H., Liu, L., He, J., 2019. On the use of quantitative schlieren techniques in temperature measurement of leader discharge channels. Plasma Sources. Sci. Technol. 28.

Further reading

WHO, 2014. Progress on Drinking Water, Sanitation and Hygiene.

Xu, J., Singh, Y.B., Amy, G.L., Ghaffour, N., 2016b. Effect of operating parameters and membrane characteristics on air gap membrane distillation performance for the treatment of highly saline water. J. Membr. Sci. 512, 73–82.

Xu, J., Singh, Y.B., Amy, G.L., Ghaffour, N., 2016c. Effect of operating parameters and membrane characteristics on air gap membrane distillation performance for the treatment of highly saline water. J. Membr. Sci. 512, 73–82.